The Measurement of Precipitation with Synthetic Aperture Radar

DAVID ATLAS

Department of Meteorology, University of Maryland, and Jet Propulsion Laboratory, California Institute of Technology, Pasadena, CA 91109

RICHARD K. MOORE

Remote Sensing and Radar Systems Laboratory, University of Kansas, Lawrence, KS 66045

(Manuscript received 20 May 1986, in final form 21 November 1986)

ABSTRACT

The radar equation for the measurement of precipitation by SAR is identical to that for a conventional radar. The achievable synthetic beamwidth, β_s, is proportional to σ_v/U, the ratio of the spread of the precipitation Doppler spectrum to the platform velocity. Thus, a small β_s can be achieved only with small σ_v or from a fast-moving vehicle such as a spacecraft. Also, the along-track resolution is variable with σ_v and is not known. Nevertheless, the reflectivity is measured correctly. A possible approach to the measurement of σ_v is noted. The C-band SAR proposed for the Shuttle Imaging Radar-C (SIR-C) mission is capable of detecting a rain rate as small as 0.5 mm h^{-1} at nadir when the beam is filled. Because the cross-track beam dimension is about 20 km wide, we suggest use of a high-resolution microwave radiometer to correct for the unfilled beam and the variation of gain across it. Alternatively, the cross-track dimension should be decreased to no more than about 5 km by increasing the antenna width and/or decreasing the wavelength.

1. Introduction

The detection and measurement of precipitation from air and space platforms is of prime importance in a wide spectrum of meteorological problems. Latent heating due to precipitation, and cooling due to its evaporation are among the primary driving forces of atmospheric motions on all scales and are thus required to understand phenomena as diverse as the dynamics of local convective storms, tornadoes, downbursts, the genesis of hurricanes and extratropical storms, and indeed, the general circulation of the global atmosphere. Climatically, adequate measurements of precipitation remain one of the key missing links in both the hydrological cycle and in the heat budget. Quantitative precipitation data are thus necessary to assist in initializing weather and climate prediction models, and to test the validity of those models. Finally, precipitation is a pivotal element in biological cycles.

There is abundant literature on the measurement of precipitation from space by means of visible, IR, and microwave radiometry and radar (Barrett and Martin, 1981; Atlas and Thiele, 1981). While some of these approaches show promise, none have been demonstrated adequately. The prospect of flying C-band synthetic aperture radars (SAR) on the European Remote Sensing Satellite ERS-1 and on the Shuttle Imaging Radar-C (SIR-C) mission stimulated us to examine the capabilities of SAR for the measurement of rain.

There is meager work on this subject. Only Atlas et al. (1977) have reported the actual detection of precipitation by airborne SAR, although we suspect that others must have done so as well, either without realizing it or not bothering to report it. With respect to quantitative analysis, only Metcalf and Holm (1979) have derived the radar equation for precipitation detection by SAR. Our purposes are 1) to provide greater physical insight into the derivation than is provided in the latter work; 2) to discuss a number of important implications which were not previously covered; 3) to provide some quantitative estimates of the detectability of rain by the C-band SAR described here; and 4) to outline some alternatives which would allow the system to be used more effectively for rainfall estimates. For ease of reference we refer to such a system as PSAR for "precipitation SAR."

2. Derivation of PSAR radar equation

We may write the conventional equation for distributed targets as

$$S_1 = \frac{P_t A_r^2 \eta c \tau \beta_v \beta_h}{32 \lambda^2 H^2} \tag{1}$$

where the symbols are defined in the Appendix and the subscript 1 refers to the conventional weather radar equation. Note that β_v and β_h are the vertical and horizontal beamwidths, respectively.

Except for the multiplier related to the shape of the beam and the antenna illumination pattern (Probert-Jones, 1962), Eq. (1) is the standard result and its behavior has been well described previously.

We proceed now to the PSAR equation. First, we must recall that the conventional equation (1) assumed the incoherent sum of the signal amplitudes or voltages corresponding to the echoes from the individual scatterers. In terms of power, such an incoherent sum is thus proportional to the number of scatterers and the average power from each. In the case of SAR, however, the full synthetic aperture can be achieved only while the targets in the pulse volume are correlated, i.e., their relative phase positions remain essentially fixed. We may assume that this is the case for times less than the decorrelation time of the echo samples in the pulse volume, as discussed later. In this case, the net voltage at the receiver is nv and the power is $n^2v^2 = n^2P$ where v and P are the individual voltages and powers received on each pulse and n is the number of pulses added along the flight track. Because noise is incoherent, the signal-to-noise ratio of a SAR is also increased by the factor n (Ulaby et al., 1982).

We see that the SAR generates an aperture larger than the real aperture by summing signals in-phase which are received sequentially rather than simultaneously, as in the case of a real aperture. This in-phase summation produces a signal-to-noise ratio which is just n times that of the incoherent sum of n signals used to form the average echo power in the conventional radar.

Using the subscript 2 for the PSAR case, we multiply S_1 by n to get

$$S_2 = \frac{P_t A_r^2 \eta c \tau \beta_v \beta_s n}{32\lambda^2 H^2}. \tag{2}$$

Note that we have now replaced the horizontal beamwidth β_h by the corresponding synthetic beamwidth β_s. For a focused SAR, Ulaby et al. (1982) show that

$$\beta_s = \lambda/2L_s \tag{3}$$

where L_s is the length of the synthetic aperture. The factor 2 appears in the denominator because the beamwidth is a function of the two-way change in phase between successive positions of the antenna at which echoes are integrated.

We may find the effective beamwidth for an assembly of moving targets such as precipitation by following the "Doppler-Beam-Sharpening Point of View" in Ulaby et al. (1982, p. 649). This is an elaboration of the method originally proposed by C. A. Wiley in the early 1950s, which was described in 1967 in a personal communication to R. K. Moore. This method was essentially what was later to become known as synthetic aperture radar.

We first consider a point target. In Fig. 1a we show the viewing geometry for the SAR calculations. The radar is on a vehicle a distance x_R back from the origin of coordinates at a height h. The coordinates of the vehicle are $(-x_R, O, h)$; those of the target are $(-x_T, y_T, O)$. The ellipse represents the half-power contour on the ground of the real beam; its width is exaggerated. The real along-track beamwidth is β_h. The range resolution along the ground is shown as r_y. Without Doppler filtering, the surface area contributing to the return at any instant is that enscribed by r_y and the real beam β_h. Also shown dashed on the surface are two isodops surrounding the target. Their spacing Δf_D is the bandwidth B_{Df} of the Doppler filter used for beam sharpening.

The target Doppler frequency is given by

$$f_{DT} = -(2u/\lambda)[(x_R - x_T)/H]. \tag{4}$$

This is positive as the radar approaches the target; the converse is also true. Neglecting the small variation in H across the real beam, f_{DT} decreases linearly with time as shown by (4) and in Fig. 1b. The time axis is also an along-track axis $x = Ut$, where U is the platform speed. For a synthetic beam with an along-track resolution of r_a and beamwidth (r_a/H), the bandwidth between isodops is

$$B_{Df} = (2U/\lambda)(r_a/H). \tag{5}$$

This is merely (4) with $r_a \approx (x_R - x_T)$.

The Doppler beam sharpening is achieved by using a narrow bandwidth filter that tracks the Doppler-shifted signal frequency from the target. In the case of the fixed target (Fig. 1b), the target is illuminated for a total duration T_a. The signal builds up in the tracking filter in time T_a. In order to resolve targets in adjacent isodop frequency bands, the transient response of the filter must be allowed to die down enough between adjacent returns. This requires that

$$B_{Df} \geq 1/T_a. \tag{6}$$

The ratio between the synthetic aperture length L_s and the time T_a to pass that length is simply the platform speed,

$$L_s = UT_a. \tag{7}$$

In other words, this is the maximum possible aperture that can be synthesized during the integration time T_a. Noting that the real horizontal beamwidth is given by $\beta_h = (\lambda/l)$, then L_s is also given by

$$L_s = (\lambda/l)H, \tag{8}$$

where l is the length of the real aperture, so that the maximum possible resolution is

$$r_a = l/2 \tag{9}$$

and the synthetic beamwidth is given by (3). This omits the aperture illumination taper factors for both the real and synthetic beams (see Ulaby et al., 1982).

Although this result has long been known, it is nevertheless remarkable in that it provides exceedingly good along-track resolution and is independent of both range and wavelength. The lack of either a range or wavelength dependence is due to the fact that the potential length of the synthetic aperture L_s is itself di-

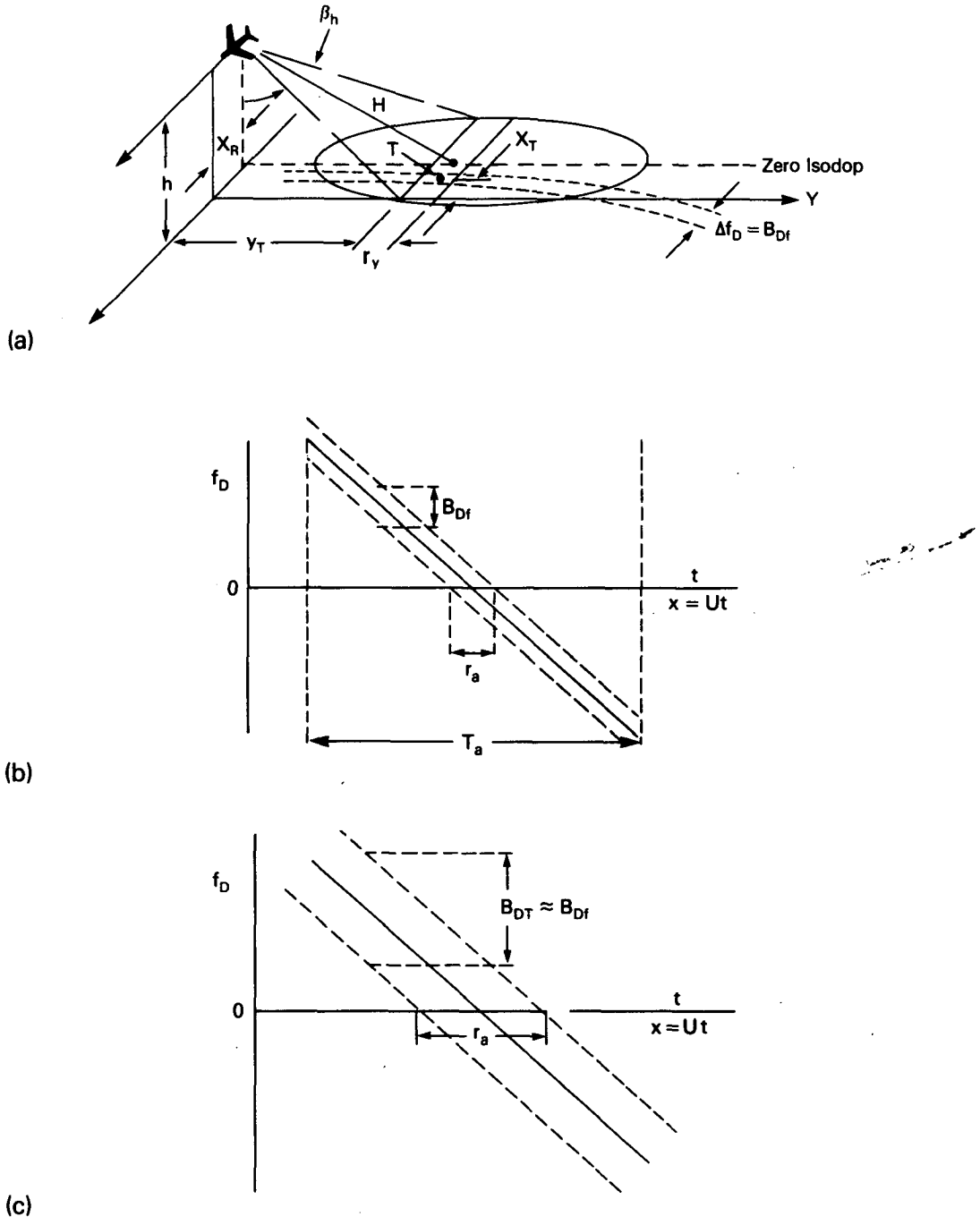

FIG. 1. (a) SAR radar geometry and isodops (dashed) on surface. (b) Doppler frequency shift versus time and/or along-track distance with tracking filter and resolution corresponding to integration time, T_a. (c) As for (b) but filter bandwidth corresponds to the reciprocal of the decorrelation time of precipitation echoes (see text).

rectly proportional to the dimension of the real beam and this increases with both range and wavelength.

With this background we may readily derive the resolution corresponding to a distributed target such as precipitation. The situation is shown in Fig. 1c. The finest Doppler resolution which can be achieved is determined by the Doppler spectral width of the target itself. In Fig. 1c, we show this as $B_{Df} = B_{DT}$ where the subscript T signifies the target. Clearly, the resolution r_a on the horizontal axis is proportional to B_{DT}, which is proportional to σ_v, the standard deviation of the precipitation velocities. In other words, coherent integra-

tion can only be maintained for the time to decorrelation, $T_a = (B_{DT})^{-1}$ (Atlas, 1964). Accordingly, the maximum synthetic aperture $L_s = UT_a = U/B_{DT}$; i.e., the greater the Doppler spread of the targets, the shorter the integration time, the smaller the synthetic aperture, and the larger the resolution element. We may write

$$B_{Df}\,(\text{precip}) = 4\sigma_v/\lambda; \tag{10}$$

substituting this into (5), we find

$$r_a = 2\sigma_v H/U. \tag{11}$$

This is unlike the behavior of the focused SAR for fixed surface targets because the along-track resolution is now a function of range once more. Using (3) with (11), we also find

$$L_s = \lambda U/4\sigma_v \tag{12}$$

$$\beta_s = 2\sigma_v/U. \tag{13a}$$

This compares to the asymptotic result of Metcalf and Holm (1979) for large rms phase variations of

$$\beta_s = 0.1874(4\pi\sigma_v/U) = 2.35\sigma_v/U. \tag{13b}$$

For present purposes we shall continue to use Eq. (13a).

To find n, the number of pulses which can be integrated coherently, we divide L_s by the distance traveled between pulses spaced T_p apart, or

$$(n-1) \approx n = L_s/UT_p = \lambda/4\sigma_v T_p. \tag{14}$$

Thus, the quantity $\beta_s n$ in (2) is

$$\beta_s n = (\lambda/2UT_p). \tag{15}$$

In essence, what this says is that the synthetic beamwidth is broadened in proportion to the Doppler spectral width of the target, σ_v, and is thus variable. On the other hand, the number of pulses which can be integrated coherently, the effective length of the synthetic aperture, L_s, and the effective coherent integration gain in S/N are inversely proportional to σ_v. Accordingly, $\beta_s n$ is independent of σ_v. This is identical to the asymptotic result of Metcalf and Holm (1979). However, they failed to recognize some of the interesting consequences of this result.

Using (15) in (2), we get the final PSAR radar equation

$$S_2 = \frac{P_t A_r^2 c\tau\eta\beta_v}{64\lambda H^2 UT_p}. \tag{16}$$

In order to compare the PSAR radar equation to that of the conventional meteorological radar equation, take the ratio of (16) to (1) so that

$$(S_2/S_1) = \lambda/(2UT_p\beta_h). \tag{17}$$

Using $\beta_h = (\lambda/l)$,

$$S_2/S_1 = l/2UT_p. \tag{18}$$

In order that $S_2 = S_1$,

$$(T_p)^{-1} = \text{PRF} = 2U/l, \tag{19}$$

which means that we must sample twice per interval of travel of the along-track dimension of the real antenna. This is precisely the condition used in SAR to avoid ambiguities in phase.

In short, the PSAR radar equation is identical to that for the conventional meteorological radar. We emphasize that the effective beamwidth increases with σ_v, the spread of the target Doppler spectrum, so that the along-track resolution is variable. However, the effective antenna gain decreases with σ_v because the number of pulses which can be coherently integrated along the track is proportional to the target coherency time and thus, inversely proportional to σ_v. Thus, the echo power is identical to that for a conventional radar with an along-track beamwidth equal to that of the real beam used in the SAR. The only exception to this occurs when the PRF exceeds that given by (19). In this case, coherent gain in S/N is achieved in proportion to the oversampling ratio so that the SAR would then have a larger S/N than a real aperture radar.

Note that in Eqs. (2) and (16) the echo power is proportional to the pulse duration. In the case of PSAR this is the entire pulse length, τ_i, and not the compressed pulse. To complete the derivation, we use the average transmitted energy per pulse (in joules)

$$P_{te}\tau_0 = P_t\tau_i, \tag{20}$$

where P_{te} is the equivalent peak power in the compressed pulse of duration τ_0 while P_t and τ_i are the actual transmitted power and pulse duration, respectively. With the standard equation for noise power,

$$N = kT_0BF, \tag{21}$$

the final result for PSAR is

$$S_2/N = \frac{P_{te}A_r\eta c\tau_0}{32H^2(kT_0F)B}. \tag{22}$$

Making the usual assumption that $B = (\tau_0)^{-1}$,

$$S_2/N = \frac{P_{te}A_r\eta c{\tau_0}^2}{32H^2kT_0F}. \tag{23}$$

Alternatively, using (20)

$$S_2/N = \frac{(P_t\tau_i)A_r\eta c}{32H^2BkT_0F}. \tag{24}$$

In short, S/N is proportional to the energy per pulse per unit bandwidth. As in the conventional case, S/N is proportional to the effective or compressed pulse width. Thus, the PSAR also achieves high-range resolution at the expense of (S/N).

Of course, since the along-track resolution for precipitation will generally be degraded from that which is achievable for a fixed target, and such high resolution is usually not required for precipitation in any case, one may use a longer pulse and narrower bandwidth. If, however, one wishes to map the surface with high

resolution and observe the precipitation simultaneously, one can regain a portion of the sensitivity which was lost due to the increased bandwidth by reprocessing the data (for precipitation), utilizing incoherent integration of the number of short pulses, m, which sum to the large pulse which satisfies one's requirements. Accordingly, the S/N of (23) or (24) is increased by $m^{1/2}$. At the same time, the number of independent signal samples in the equivalent long pulse will be increased by m and the standard deviation of the estimated average echo intensity will be reduced by $m^{1/2}$, thus improving the accuracy of the reflectivity measurements.

When we include the Probert-Jones factor of 0.445 as typical, a factor L for system losses, and the two-way attenuation by rain, κ, we obtain the final form of (24):

$$\frac{S_2}{N}=\frac{0.445P_t\tau_i A_r\eta cm^{1/2}L\kappa}{32H^2N}. \tag{25}$$

3. Beamwidth

Metcalf and Holm (1979) have also shown that, provided both the real and expected synthetic gain patterns are both approximately Gaussian, the effective radiation pattern is the product of the real and synthetic beams. Accordingly, it is readily shown that the effective beamwidth

$$\beta_e=\frac{\beta_r\beta_s}{(\beta_r^2+\beta_s^2)^{1/2}} \tag{26}$$

where the subscripts are e for effective, r for real, and s for synthetic. Thus, $\beta_e \approx \beta_s$ where $\beta_s < \beta_r/3$. Using $\beta_r \approx \lambda/l_h$ and (13a) for β_s, we find that this occurs when

$$\sigma_v \leqslant \lambda U/6l_h. \tag{27}$$

Table 1 shows the maximum values of σ_v which satisfy the condition of (27) for C-band SARS for aircraft and spacecraft. For the aircraft SAR, the limiting σ_v under which we set $\beta_e \approx \beta_s$ is only about 0.9 m s^{-1}. However, for the spacecraft system, we achieve the synthetic apertures for all σ_v up to about 6 m s^{-1}. In short, the much faster-moving spacecraft can tolerate a much broader Doppler spectrum and still achieve a synthetic beamwidth less than ⅓ that of the real beam. On the other hand, the aircraft SAR requires a very quiet atmosphere with $\sigma_v < 0.9$ m s^{-1} to attain a similar result. In Fig. 2 we plot β_e versus β_s for a variety of values of β_r. For all practical purposes $\beta_e \approx \beta_s$ for all

TABLE 1. Maximum Doppler spectral width (σ_v) for which the effective SAR beamwidth is the synthetic beamwidth.

	λ (cm)	l_h (m)	U (m s^{-1})	σ_v (m s^{-1})
Aircraft	5.7	1.5	150	0.88
Spacecraft	5.7	12	7×10^3	5.5

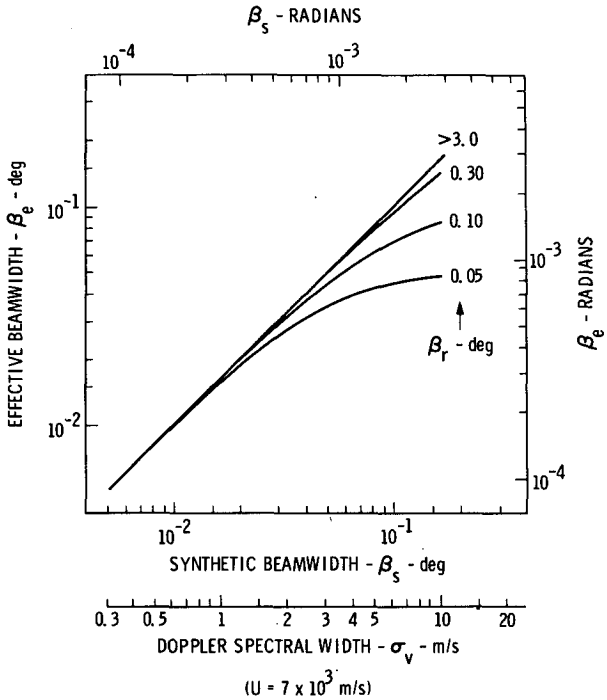

FIG. 2. Effective, synthetic, and real beamwidths. Bottom scale is Doppler spectral width for vehicle velocity of 7 km s^{-1}.

$\beta_r > 0.3°$ if $\beta_s < 0.2°$. As β_r decreases, however, the largest value of β_s at which this is true becomes smaller. Because β_s is a function only of the Doppler spectral width, σ_v, the abscissa in Fig. 2 also shows a scale of σ_v for a spacecraft velocity of 7×10^3 m s^{-1}.

The synthetic beamwidths which are attained for the aircraft and spacecraft configurations, and the corresponding along-track resolutions at the surface assuming the given altitudes are shown in Table 2.

The beamwidths in Table 2 may be compared to real beams of 0.27 deg for a spacecraft antenna length of l = 12 m or 1.64 deg for an aircraft with l = 2 m,

TABLE 2. Synthetic beamwidths and along-track resolution for aircraft and spacecraft SARs (independent of wavelength).

	Precipitation Doppler spread, σ_v (m s^{-1})			
	0.5		5	
	(rad)	(deg)	(rad)	(deg)
Aircraft: Speed—150 m s^{-1}; alt—12 km				
Beamwidth	6.67×10^{-3}	0.382	6.67×10^{-2}	3.82
Footprint (m)	81.3		813	
Spacecraft: Speed—6.7×10^3 m s^{-1}; alt—255 km				
Beamwidth	1.43×10^{-4}	8.18×10^{-3}	1.43×10^{-3}	8.18×10^{-2}
Footprint (m)	36.5		365	

respectively, both at $\lambda = 5.7$ cm. For the fast-moving spacecraft, the synthetic beam is greatly reduced even for the larger σ_v. For the aircraft, the resolution is improved only for the smaller σ_v. Since σ_v is largely dependent on the size of the real aperture in the across-track direction and the wind shear across the corresponding vertical beamwidth, it is important to make this antenna dimension as large as possible. Later, we shall show why the unambiguous interpretation of the reflectivity and velocity measurements also require a narrow vertical beam.

It is interesting that the radar equation (22)–(24) is dependent only upon the dimensions of the real aperture and not upon either the synthetic aperture or beamwidth. However, since the latter is a function of σ_v, which varies with the nature of the precipitation and the associated windfield and turbulence, the along-track resolution will be variable and unknown. In order to obtain the best resolution everywhere, it is clear that one will have to process the PSAR data either in some sort of adaptive mode or with a variety of integration times. The optimum time for each volume element will be that which corresponds to the target coherency time. For integration beyond this time neither the S/N nor the resolution will increase any further. This suggests the possibility of devising a means of adaptively controlling the duration. If this works, the tagging and mapping of the optimum integration times would also provide a display of the breadth of the Doppler spectral width.

While it may be somewhat disturbing to the analyst to see the image crispness vary from point to point, the reflectivity and associated precipitation rate will be measured correctly provided only that the vertical beam dimension is filled. This is another important reason to keep the vertical beamwidth as small as possible. We suggest a reasonable cross-track resolution later.

4. Precipitation sensitivity of SIR-C SAR

We now compute the minimum detectable reflectivity and rainfall rate for the C-band Shuttle Imaging Radar (SIR) planned for the SIR-C mission. The system parameters are given in Table 3. These are nominal values and are subject to change. We start with Eq. (25) and calculate the S/N versus rain rate for a single pulse assuming beam filling, $m = 1$, and $\kappa = 1$ (i.e., no attenuation). To convert reflectivity η to the reflectivity factor, Z, and then to rain rate, R, we use

$$\eta = 0.36 \times 10^{-12} Z, \tag{28}$$

and

$$Z = 300 R^{1.5} \tag{29}$$

or

$$R = 4.41 \times 10^{6} \eta^{2/3} \tag{30}$$

where the units are η in cm^{-1}, Z in (mm)^6 m^{-3}, R in mm h^{-1}, and the η–Z relation is for Rayleigh scatter at $\lambda = 5.3$ cm. The result is

TABLE 3. System characteristics of SIR-C C-Band SAR.

Parameter	Symbol	Value
Wavelength	λ	5.3 cm
Peak transmission power	P_t	2.5 kW
Pulse widths:		
actual	τ_i	34 μs
compressed	τ_0	80 ns
Pulse repetition frequency	(PRF)	1800 Hz (max)
Pulse repetition period	T_p	0.556 ms (min)
Antenna gain (real)	G_r	42.1 dB
Effect. antenna aperture	A_r	3.63 m^2
Antenna dimensions:		
length	l_h	12.1 m
width	l_v	0.8 m
System loss	L	2 dB
Receiver bandwidth	B	12.5 MHz
Noise power	N	−133 dBW
Shuttle		
height	H	255 km
speed	U	6.7 km s^{-1}
Nadir footprint dimensions:		
along-track (real)	D_h	1.1 km
cross-track	D_v	16.7 km

$$(S/N) = 2.67 R^{1.5} \quad \text{(single pulse)}. \tag{31}$$

The result is shown as case A in Table 4. The minimum detectable rain rate for $(S/N) = 1$ at a range of 255 km is 0.52 mm h^{-1}, assuming beam filling. The corresponding minimum detectable reflectivity factor ($10 \times \log Z_{\min}$) is 20 dBZ.

Table 3 shows that the cross-track footprint dimension is 16.7 km when the shuttle is tilted so that the beam is pointing at nadir. Also, the maximum along-track footprint dimension at nadir is 1.12 km, corresponding to the width of the real beam. The S/N is independent of the along-track dimension according to our earlier discussion, provided we have some degree of aperture synthesis and the storm dimension is never less than 1.12 km. On the other hand, the 16.7-km cross-track dimension may not be filled. Case B in Table 4 assumes that only ¼ of this dimension is filled, thereby increasing $Z_{\min}$ by 6 dB and increasing $R_{\min}$ by a factor of 2.5 to 1.3 mm h^{-1}.

Because the cross-track beamwidth is so large, it would be desirable to decrease it by a factor of about 4, thus decreasing the cross-track width of the nadir footprint to 4.2 km. This requires increasing the antenna width and area four-fold, thus increasing (S/N) by the same amount. This is case C in Table 4 with $R_{\min} = 0.21$ mm h^{-1}. Note also that (31) and cases A and B of Table 4 are based on the single high-resolution pulse length of 12 m. For most meteorological purposes we can tolerate a resolution as crude as 300 m. We can thus choose m = 25 for incoherent integration. If we now combine the increased antenna width with this incoherent integration, the sensitivity increases by a factor of 20 or 13 dB. This corresponds to case D in Table 4, with a minimum detectable rain rate of 0.07 mm h^{-1}. This is remarkably good.

TABLE 4. Minimum detectable rain rates and reflectivities for SAR at $S/N = 1$ and range of 255 km for various configurations.

Case	Features	10 log(Z_{min}) (dBZ)	R_{min} (mm h^{-1})
A	SAR as in Table 3; beam filled	20	0.52
B	SAR as in Table 3; ¼ beam filled	26	1.30
C	Increase antenna width by 4	14	0.21
D	Case C with 25-fold incoherent integration	7	0.07
E	Increase antenna width by 2 and decrease wavelength by ½	5	0.05

5. Geometric considerations

It is clear that a cross-track footprint dimension (y) of 16.7 km will often exceed the dimensions of showers and thunderstorms. Accordingly, unless we have some independent information concerning the y storm dimension, reflectivity measurements will be erroneous. The geometry is illustrated in Fig. 3. Figure 3a shows the scaled geometry for a flat earth assumption, a vertical beamwidth of 4 deg, and a storm height of 15 km. In Fig. 3b we have exploded the lowermost segment of the beam, which is shown hatched in Fig. 3a. The ordinate is now height above the flat earth. The dashed lines are segments of constant range circles.

Superimposed on the geometry of Fig. 3b is a vertical section of a convection storm not unlike the real thing. The contours are equivalent reflectivity factors 10 log(Z) in dBZ and we have omitted the lower reflectivities to avoid complicating the figure.

If we use the SCANSAR mode (Moore et al., 1981) in which the beam is switched sequentially over the five beamwidths, the total swath width is 93 km on each side of the spacecraft. The y dimension of the 4-deg beam is close to 20 km at a nadir angle $\theta = 18$ deg. We have outlined the area in which the lower edge of the beam just intersects the earth's surface (point A), and the assumed storm top at 15-km height (point B). The intersections of constant range circles through A and B with the far side of the beam at 20° nadir angle give points D and C, respectively. We see that the beam-filling problem is compounded by the tilt of the constant range circles so that only those portions of the storm cell which fall in the area AEFD will be measured correctly, assuming uniform reflectivity across a range element between H and $H + dH$ where dH is the range resolution and within the bounds of the storm or beamwidth, whichever is smaller, but this is unlikely to be achieved in reality. When the reflectivity varies across the beam as shown, the average reflectivity is given approximately by

$$\bar{\eta} \approx \frac{dH}{\theta\phi} \int\int G(\theta', \phi')\eta(\theta', \phi')d\theta' d\phi', \qquad (32)$$

where θ' and ϕ' are the along- and cross-track angles, respectively, referenced to the beam center. The limits on θ' and ϕ' are either the boundaries of the beam or the storm, whichever is smaller. Since the reflectivity in convective storms varies sharply in all directions, it is usually sufficient to restrict the limits of integration to the region in which the product $G\eta$ is within -10

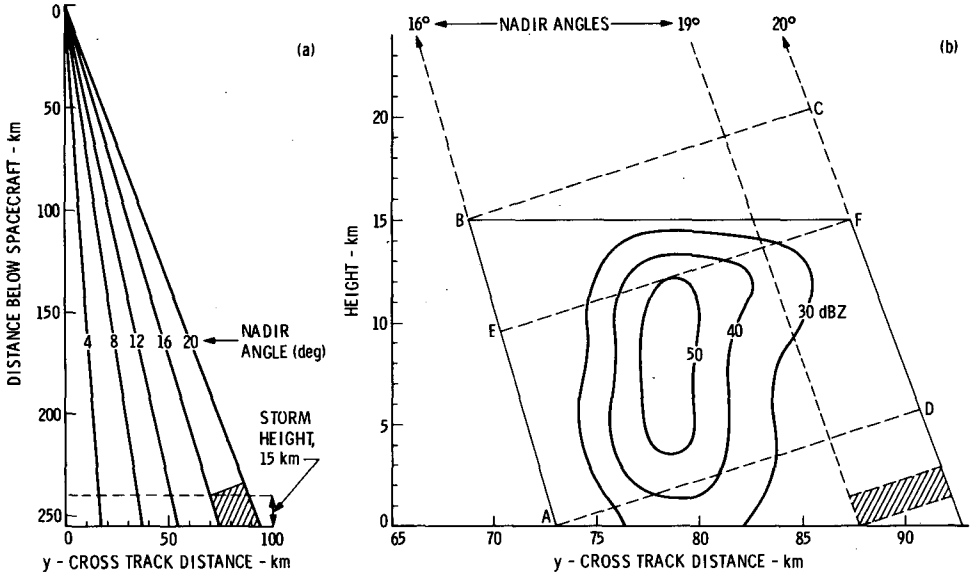

FIG. 3. (a) Scaled geometry for five beamwidths from 225 km orbit; (b) exploded view of hatched area in (a).

dB of its maximum value. Unfortunately, it is possible to do this only when one knows the finescale distribution of η. This can only come from high-resolution observations from ground or airborne radars or models thereof which permit us to simulate the SAR observations.

On the other hand, the retrieval of mean reflectivity or precipitation rates from the SAR data can only resort to cruder methods. One approach is to utilize a high-frequency microwave radiometer to image the dimensions of the precipitation over the ocean and their actual locations within the large cross-track footprint. (Precipitation is more readily observed over ocean than land because of the contrast against the cold and relatively constant microwave brightness of the ocean.) The location of the storm cell then determines the effective SAR antenna gain at that position. The cross-track storm radiometric dimension also determines the fraction of that beam dimension which is filled. To first order, the measured reflectivity is given by

$$\eta_m \approx G/D_v \int_{-\delta/2}^{+\delta/2} \eta dy = G\bar{\eta}\delta/D_v, \qquad (33)$$

where G is the antenna gain at the actual cell position, δ is the actual y cell dimension, D_v the full beam dimension, and $\bar{\eta}$ is the average reflectivity over δ which one desires to measure. Conversion to the rain rate can be made by (30). If we use a 35-GHz radiometer with a 1-m dish, the footprint will be about 2.2 km from orbit altitude of 255 km. This will tend to enlarge the cell dimensions slightly. One can go through the exercise of deconvolving the actual cell dimension from that which is measured, or simply subtract the beamwidth. This will introduce some error in δ and the computed values of $\bar{\eta}$ and R. Note that a check on the radiometric cell broadening may be made in the along-track direction because that radar resolution is better than that of the radiometer. Of course, this approach is crude because the radiometer will integrate vertically and thus indicate the maximum storm dimension anywhere in depth rather than the size at the desired height.

In order to improve the situation, and possibly to use the SAR without the aid of the radiometer, we have considered an antenna with a 1 deg vertical beamwidth. The area corresponding to this beam is shown hatched in Fig. 3b from the lowest corner of the beam on the left which just touches the surface to its highest on the right. At the angles shown, a constant range element encompasses a height range of only 1.44 km, decreasing to zero at nadir. This geometry thus permits us to estimate the rain rate with fewer assumptions as to cell size and homogeneity. It also permits extending the rain observations down to within 1.4 km of the surface or less over the entire 93-km half-swath without contamination by surface echo clutter. The 5-km horizontal beamwidth is still somewhat deficient to resolve the reflectivity pattern of the storm cell shown in Fig. 3b, but it should allow greatly improved reflectivity and rainfall estimates. We may decrease the cross-track beam dimension by a four-fold increase in antenna width at C band, or by decreasing the wavelength by a factor of 2 and doubling the antenna width. Although the move to X-band will result in some attenuation, the tradeoff may be necessary to keep the antenna width within reason. This situation is shown by case E in Table 4, with a minimum detectable rain rate of 0.05 mm h^{-1}, neglecting attenuation.

If we have a 1-deg vertical beamwidth and corresponding 5-km cross-track footprint, it is hardly necessary to seek the very high along-track resolution possible with the synthetic aperture. It is then worth considering using the system with its real beamwidths of 1.13 km along-track in the manner of a conventional radar. Assuming a ground swath width of ±93 km corresponding to ±20 deg, we would have to cover 40 beamwidths in the time the spacecraft travels 1.13 km, or (1.13/7) = 0.161 sec. At the maximum PRF of 1800 Hz, we then have

$$J = \frac{0.161 s}{\text{swath}} \times \frac{1800 \text{ pulses}}{s} \times \frac{1 \text{ swath}}{40BW}$$

$$J = 7.25 \text{ pulses}/BW.$$

Depending upon the Doppler spectrum variance and decorrelation time of the precipitation echoes, a fraction of these will be independent; say 3 to 5. By averaging over five range gates (each of 12-m depth) we contain 15 to 25 independent samples, resulting in a good estimate of echo power and a range resolution of 60 m. In short, we have a very sensitive radar with reasonable resolution.

Unfortunately, with the planned C-band SAR on SIR-C we will have to make do with a vertical beamwidth of about 4 deg. This will require the use of the auxiliary radiometer to estimate the cross-track dimension of the precipitation cells and permit useful rainfall estimates.

6. Summary and conclusions

The radar equation for the measurement of precipitation by SAR is identical to that for a conventional radar. This was also found earlier by Metcalf and Holm (1979) using a different approach. The synthetic beamwidth, β_s, achievable by SAR on precipitation is proportional to σ_v/U, the ratio of the spread of the target Doppler spectrum to the platform velocity. This means 1) a small β_s can be achieved only with small σ_v (i.e., in a nonturbulent, low-shear environment) or from a fast-moving vehicle such as a spacecraft; and 2) the along-track resolution is variable with σ_v so that the crispness of the images depends upon the precipitation and associated winds. Nevertheless, the reflectivity is measured correctly because the number of pulses which

can be integrated coherently, and thus the synthetic gain, is inversely proportional to σ_v. This assumes that the cross-track beamwidth is filled. A possible approach for the estimation of σ_v is suggested.

We find that the C-band SAR proposed for the Shuttle Imaging Radar-C (SIR-C) mission is capable of detecting a rain rate as small as 0.5 mm h^{-1} at nadir with a range resolution of 12 m if the cross-track beamwidth of 16.7 km is filled, or 1.3 mm h^{-1} if only ¼ of the beam is filled. Incoherent integration to an effectively longer pulse enhances the sensitivity.

From the 255-km orbit of the Shuttle, the 4-deg cross-track beamwidth of the SAR will cover a swath of 93 km on one side in five steps of about 19 km each. Many storms will not fill this dimension. We suggest use of a high-resolution microwave radiometer to estimate the actual storm dimension and locate it within the radar beam for the proper choice of antenna gain. Alternatively, one may decrease the cross-track beam dimension to about 5 km by a four-fold increase in the antenna width or a combination of decreasing the wavelength by a factor of 2 (to 2.65 cm) and increasing the antenna width twofold. This would allow improvd rain rate estimates without the need of the radiometer. However, a move to the shorter wavelength incurs the risk of attenuation errors.

Acknowledgments. The lead author appreciates stimulating discussions with Drs. Charles Elachi, Daniel Held, and Rolando Jordan of the Jet Propulsion Laboratory, California Institute of Technology, where part of this work was conducted. We are also grateful to Mrs. Charlene Mann and Mrs. Corinne Preston of the Department of Meteorology, University of Maryland for processing the manuscript. The research was also supported in part under NASA Grant NAG 5/542.

APPENDIX

List of Symbols

A_r	Antenna area
B	Bandwidth
$D_{h,v}$	Footprint dimensions, h—horizontal, v—vertical
F	Noise figure
$G_{t,r}$	Antenna gain; t—transmit; r—receive
H	Slant range
H_o	Orbital height
J	Number of pulses per beamwidth
L	System loss
L_s	Length of synthetic aperture
N	Noise power
PRF	Pulse repetition frequency
P_t	Transmitted power
R	Rainfall rate
S	Received echo power
T_a	Integration or coherency time
T_0	Receiver noise temperature
T_p	Pulse repetition period
U	Platform velocity
V	Pulse volume
Z	Radar reflectivity factor
c	Speed of light
f_D	Doppler frequency
k	Boltzman constant
$l_{h,v}$	Length of real aperture, h—horizontal, v—vertical
m	Number of pulse lengths integrated incoherently
n	Number of pulses integrated coherently
r_a	Along-track resolution
x	Along-track distance
y	Cross-track distance
$\beta_{h,v,e,r,s}$	Beamwidth; h—horizontal, v—vertical, e—effective, r—real, s—synthetic
κ	Atmospheric attenuation
λ	Wavelength
δ	Cross-track cell dimension
η	Radar reflectivity
ϕ	Nadir angle to x, y coordinates on surface
σ	Radar cross section of equivalent isotropic scatterer
σ_v	Standard deviation of Doppler spectrum of targets
$\tau_{0,i}$	Pulse duration; 0—compressed; i—actual
θ	Cross-track angle to x, y coordinates on surface

REFERENCES

Atlas, D., 1964: Advances in radar meteorology. *Advances in Geophysics,* Vol. 10, H. E. Landsberg, Ed., Academic Press, 317–478.

——, and O. Thiele, 1981: Precipitation measurements from space. Workshop Rep. NASA/Goddard Space Flight Center, 431 pp.

——, C. Elachi and W. E. Brown, Jr., 1977: Precipitation mapping with an airborne synthetic aperture imaging radar. *J. Geophys. Res.,* **82,** 3445–3451.

Barrett, E. C., and D. W. Martin, 1981: *The Use of Satellite Data in Rainfall Monitoring.* Academic Press, 340 pp.

Metcalf, J. I., and W. A. Holm, 1979: Meteorological applications of synthetic aperture radar. Final Rep. Proj. A-2101 Eng. Experiment Station, Georgia Inst. of Technology, 33 pp.

Moore, R. K., J. P. Claassen and Y. H. Lin, 1981: Scanning synthetic aperture radar with integrated radiometer. *IEEE Trans. Aerospace Electron. Sys., AE-17,* 697–708.

Probert-Jones, J. R., 1962: The radar equation in meteorology. *Quart. J. Roy. Meteor. Soc.,* **88,** 485–495.

Ulaby, F. T., R. K. Moore and A. K. Fung, 1982: *Microwave Remote Sensing.* Vol. II, Addison-Wesley, 457–1064.